Synthesis, growth mechanism, and morphology control of $LiFe_{1/3}Mn_{1/3}Co_{1/3}PO_4$ via a microwave-assisted hydrothermal method

Kunpeng Wang,[a] Alexander Ottmann, and Jianxiu Zhang
Kirchhoff Institute for Physics, Heidelberg University, Heidelberg D-69120, Germany
Hans-Peter Meyer
Institute of Earth Sciences, Heidelberg University, Heidelberg D-69120, Germany
Rüdiger Klingeler
Kirchhoff Institute for Physics, Heidelberg University, Heidelberg D-69120, Germany; and Centre for Advanced Materials, Heidelberg University, Heidelberg D-69120, Germany

(Received 25 November 2014; accepted 23 February 2015)

$LiFe_{1/3}Mn_{1/3}Co_{1/3}PO_4$ (LFMC) has been synthesized by a microwave-assisted hydrothermal technique. During the crystal growth, two evolutionary routes coexist and compete with each other after the nuclei have been stably formed. One of them is the continuous growth of single particles and the other one is agglomeration. The size and morphology of the products are determined by the interplay of the two competing routes. The growth morphology is quantitatively analyzed from first principle calculations. A phase diagram is constructed, which guides to control the morphology by adjusting C_M and pH. Static magnetic properties imply long range antiferromagnetic order below $T_N = 39$ K and a paramagnetic Curie–Weiss-like behavior with $\theta = 75$ K and $p_{eff} = 5.51\ \mu_B$ at high temperatures. Cyclic voltammetry shows two distinct peaks corresponding to the Fe^{2+}/Fe^{3+} and Co^{2+}/Co^{3+} redox couples, respectively, whereas the Mn^{2+}/Mn^{3+} redox couple is not observed due to its sluggish kinetics induced by the Jahn–Teller effect of Mn^{3+}.

I. INTRODUCTION

As one of the most efficient portable energy storage systems at the moment, rechargeable lithium-ion batteries based on electrochemical intercalation materials are crucial to realize electric vehicles which are able to reduce the CO_2 emissions by petroleum-fueled internal combustion engine vehicles.[1] To meet the challenging requirements, extensive research has been underway on cathode materials since they are the bottleneck, hindering improvements with regard to energy density, cell voltage, capacity, cyclic performance, lifetime, etc.[2–4] Olivine-structured $LiMPO_4$ (M = Fe, Mn, Co, and Ni) with a theoretical specific capacity of around 170 mAh g^{-1} has recently attracted increasing interest as a promising cathode material for rechargeable lithium-ion batteries due to as well low cost as safety benefits.[5–8] However, the electrochemical performance of pristine phosphates still needs to be improved, even though there has been huge progress in the case of $LiFePO_4$.[5] Here, poor rate capabilities caused by low electrical conductivity and low ionic diffusivity have been overcome by nanosizing and carbon coating.[9,10] In contrast, the other olivine-structured materials with a single transition metal ion (M = Mn, Co, and Ni) have not reached commercial applicability so far. For example, there are severe issues of capacity fading for $LiMnPO_4$ because of the Jahn–Teller effect of Mn^{3+} ions.[6,11,12] Besides other issues, the commonly used electrolytes are instable at the high operating voltages of $LiCoPO_4$ and $LiNiPO_4$ versus lithium.[13–15] More recently, solid solutions of multicomponent olivine-structured phosphates are getting more and more attention due to their enhanced energy density or increased rate capability compared to their single component counterpart. The $LiFe_{1-x}Mn_xPO_4$ system has been studied from the beginning as a route to exploit the higher potential of the Mn^{2+}/Mn^{3+} couple versus lithium compared to Fe^{2+}/Fe^{3+}.[5,16,17] The synthesis and extensive investigation of $LiFe_{1/3}Mn_{1/3}Co_{1/3}PO_4$ (LFMC) have been recently done by several groups[18–21] and the results imply that the electrochemical performance is strongly affected by the synthesis conditions and synthesis methods. In this study, we report on the synthesis of $LiFe_{1/3}Mn_{1/3}Co_{1/3}PO_4$ by a microwave-assisted hydrothermal method and study the resulting morphologies upon systematic variation of the pH value and the transition-metal-ion concentration (C_M) in the reactant. Hydrothermal technology is a suitable tool to meet the requirements of a size- and shape-controlled

---

Contributing Editor: Michael E. McHenry
[a] Address all correspondence to this author.
e-mail: kunpeng.wang@kip.uni-heidelberg.de
DOI: 10.1557/jmr.2015.63

synthesis for battery materials.[22] In case of the olivine-type phosphates, it has been utilized since the pioneering work in the group of Whittingham et al.[23] to synthesize a broad range of mixed transition metal compounds[24] and to manipulate the particle morphology by changing the synthesis parameters, in particular the pH value.[25–31] The microwave-assisted approach accelerates the crystallization kinetics, shortens the reaction time, and improves the efficiency of the technique[32] and it has successfully been applied for all $LiMPO_4$ (M = Fe, Mn, Co, Ni) materials.[33,34]

Our systematic investigations of the synthesis products depending on the initial pH value and transition metal ion concentration of the reactant show that two evolutionary routes coexist during the crystal growth and compete with each other after the nuclei have been stably formed. The morphologies of the products are determined by the interplay of these two competing routes. In addition, the morphology is quantitatively analyzed by means of first principles methods, using the Hartman–Perdok approach. A crystalline and agglomeration phase diagram is constructed. Furthermore, the magnetic and electrochemical properties are reported.

II. EXPERIMENTAL AND THEORETICAL METHODS

LFMC has been hydrothermally synthesized by means of a microwave-assisted approach. Firstly, $LiCH_3CO_2{\bullet}2H_2O$, $Fe(CH_3CO_2)_2$, $Mn(CH_3CO_2)_2{\bullet}4H_2O$, $Co(CH_3CO_2)_2{\bullet}4H_2O$, and $(NH_4)_2HPO_4$ were dissolved in deionized water under stirring in an off-stoichiometric ratio of 9:1:1:1:3 with respect to the ratio of Li, Fe, Mn, Co, and P. All chemicals were analytically pure and were used directly without purification. The concentration of the transition metal ions (C_M) in the solution was adjusted to a value between 0.03 and 0.12 mol/L. Then, either diluted ammonia or acetic acid (100%) was separately added drop-wise under stirring to adjust the pH value of the solution, starting around 6, in the range from 5 to 11. 15 mL of the solution was transferred into a 30 mL quartz vial of the microwave furnace (Anton Paar Monowave 300). The reaction temperature of 220 °C was reached within a ramping time of 10 min and kept for 20 min before the sample was cooled down below 55 °C. The gained precipitate was rinsed six times with distilled water and ethanol, respectively, to remove residual precursors and solvents. The resulting powder was dried in air at 70 °C for 24 h under ambient pressure.

The products were studied by x-ray powder diffraction by means of a Siemens D500 (Germany), utilizing Cu $K_{\alpha1}$ and Cu $K_{\alpha2}$ radiation ($\lambda_{1/2}$ = 1.54056/1.54433 Å). The diffraction patterns were taken in the range from 10 to 80° with a step size of 0.02° and an integration time of 1 s per step. The morphology of the products was determined with a Zeiss LEO 1530 scanning electron microscope (SEM; Germany). The temperature dependence of the static magnetic susceptibility $\chi = M/B$ was measured after cooling in zero magnetic field (ZFC) in an applied external magnetic field of $B = 0.5$ T from 2 to 350 K by means of a Quantum Design MPMS XL5 SQUID magnetometer.

For electrochemical studies, the electrode material has been prepared from a slurry of 75 wt% pristine powder, 20 wt% carbon black (Timcal), and 5 wt% polyvinylidenfluoride (PVDF) binder (Solvay Plastics) with 1-methyl-2-pyrrolidone (NMP) as a solvent (Sigma–Aldrich) (see Ref. 35). The slurry was pasted on an Al-mesh (diameter ~10 mm), dried for 24 h at 70 °C in a vacuum oven, and pressed. The cells were assembled inside a glove box under argon atmosphere ($O_2/H_2O < 2$ ppm). The positive LFMC electrode was separated by two pieces of Whatman borosilicate glass fiber from the negative electrode which consisted of a metallic lithium disk on a nickel current collector (diameter ~8 mm). As electrolyte, a 1 M LiPF6 salt solution in a 1:1 mixture of ethylene carbonate (EC) and dimethyl carbonate (DMC) was used. Cyclic voltammetry (CV) measurements were carried out by using a VMP3 multichannel potentiostat (Bio-Logic) in a climate chamber at 298 K. The scan rate was fixed at 0.1 mV s^{-1} in the voltage range from 2.60 to 5.25 V.

To study the growth process and the morphology in detail, the attachment energies and slice energies of different growth layers with thickness d_{hkl} have been calculated based on density-functional theory with the SIESTA implementation.[36] The total energy ultrasoft pseudopotential[37] method was used. The cutoff energy of the plane-wave basis function was set to be 400 eV, yielding a convergence for the total energy of better than 0.01 eV/atom. All energy calculations were carried out as described in detail in Ref. 38 with the generalized-gradient approximation (GGA) using the Perdew–Burke–Ernzerhof model[39] for electron exchange and correlation. Based on an experimental $LiFePO_4$ structure (ICSD-161479), we have constructed a repeated supercell containing 84 atoms (12 $LiFePO_4$ f.u.) with lattice vectors $\boldsymbol{A} = a\boldsymbol{i}$, $\boldsymbol{B} = (b\boldsymbol{j} + c\boldsymbol{k})$, and $\mathbf{C} = (-b\boldsymbol{j} + 2c\boldsymbol{k})$, where $a = 10.307$ Å, $b = 5.989$ Å, and $c = 4.700$ Å are the lattice constants of the conventional unit cell of $LiFePO_4$. The supercell was used to define the positions for the well mixed Fe^{2+}, Mn^{2+}, and Co^{2+} ions in LFMC [Fig. 1(a)]. For the attachment energy calculations, we took the {101} slice as an example. Firstly, a slab consisting of five growth slices was constructed and then the top {101} slice with the interplanar distance $d_{hkl} = 4.276$ Å was shifted to 100 Å away from the slab surface to eliminate the interaction between the slab and the slice [Fig. 1(b)]. Lattice energies of the slab and the separated slice were calculated based on this model, and then the attachment energies,[40] defined as the energy released on attachment of a growth slice to a growing crystal surface, have been deduced.

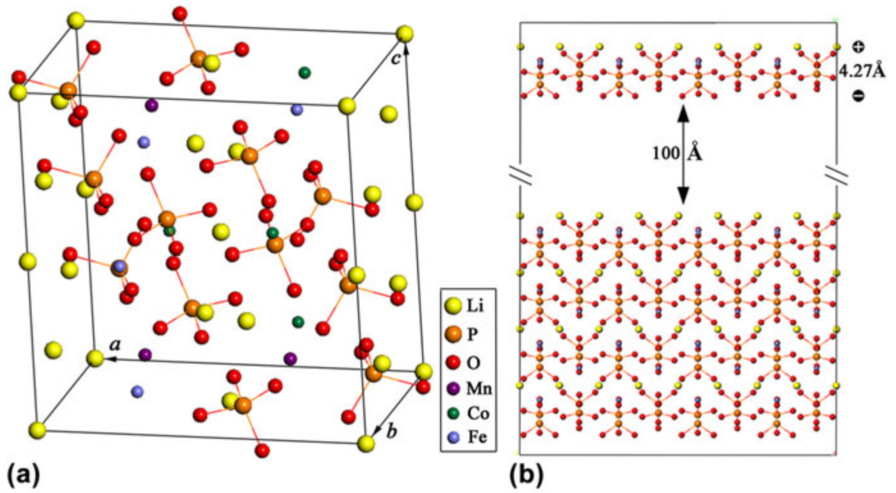

FIG. 1. (a) LFMC supercell, and (b) slab consisting of four growth slices and one separated slice.

III. RESULTS AND DISCUSSION

A. Structure and morphology analysis

Figure 2(a) shows the x-ray diffraction (XRD) patterns of the as-prepared products synthesized at different pH and C_M values. Except for two samples, made at C_M = 0.03 mol/L and pH 5 and 6, all materials are crystalline and the main peaks in the XRD patterns can be assigned to olivine-structured LFMC with space group *Pnma*. The synthesized materials can be merged into four groups (see regimes I–IV at the left ordinate in Fig. 2) and a crystalline phase diagram (see Fig. 3) can be deduced with respect to the corresponding pH and C_M values. The four groups are: regime I with noncrystalline material [marked with squares in Fig. 2(a)], regime II exhibiting pure LFMC (stars), region III where LFMC appears with $(Fe,Mn)_3(OH)_2(PO_4)_2$ impurities (circles), and region IV comprising LFMC with Li_3PO_4 impurities (triangles). The synthesis phase diagram shows that the pH value and precursor concentration are fundamental parameters for the microwave-assisted hydrothermal synthesis of LFMC. At a low transition metal precursor concentration of C_M = 0.03 mol/L and pH $\leq$ 6.5 (region I), amorphous material is the main constituent of the as-prepared product. Increasing the pH value in the regime 6.5 < pH < 9.5 at fixed C_M = 0.03 mol/L yields crystalline LFMC with however $(Fe,Mn)_3(OH)_2(PO_4)_2$ impurities (region II), which disappear upon further increase of pH, i.e., at pH $\geq$ 10. The crucial effect of precursor concentration is evident as well: At pH $\geq$ 10 and $C_M \geq$ 0.06 mol/L, Li_3PO_4 appears in addition to the main phase LFMC. Note, that the promotion of a Li_3PO_4 impurity phase at high pH values has also been observed for the synthesis of $LiMnPO_4$ in Ref. 21. Finally, there is an extended region (II), where phase pure synthesis of LFMC is observed, roughly ranging from top-left (low pH, high C_M) to bottom-right (high pH, low C_M) in Fig. 3.

The lattice parameters of all crystalline samples are refined by the GSAS program[41] [see Fig. 2(b)] and compared to the previous reported results [marked with open circles in Fig. 2(b)]. The average lattice parameters of our samples are a = 10.331 Å, b = 5.993 Å, and c = 4.723 Å, which results in V = 292.45 $Å^3$. These values are in good agreement with Ref. 18 (a = 10.337 Å, b = 6.008 Å, c = 4.717 Å, V = 292.95 $Å^3$), Ref. 21 (a = 10.329 Å, b = 6.017 Å, c = 4.711 Å, V = 292.79 $Å^3$), Ref. 20 (a = 10.328 Å, b = 6.012 Å, c = 4.711 Å, V = 292.54 $Å^3$), and Ref. 42 (a = 10.326 Å, b = 6.011 Å, c = 4.713 Å, V = 292.53 $Å^3$), but larger than those reported in Ref. 43 (a = 10.208 Å, b = 5.945 Å, c = 4.689 Å, V = 284.64 $Å^3$) and Ref. 19 (a = 10.310 Å, b = 5.990 Å, c = 4.701 Å, V = 290.26 $Å^3$). The lattice parameters of our samples are comparable to the average lattice parameters (a = 10.338 Å, b = 6.009 Å, c = 4.718 Å, V = 293.10 $Å^3$) Ref. 18 of the end members $LiFePO_4$, $LiMnPO_4$, and $LiCoPO_4$, which is an indication of complete solubility of the ions Fe, Mn, and Co. We find that the lattice parameters and unit cell volume of the pure LFMC [see region II in Fig. 2(b)] are a function of the synthesis pH values, decreasing with increasing pH from 4 to 7, then increasing from 7 to 10. While there are clear effects on the lattice parameters in the impurity region III, and the effects in region IV with Li_3PO_4 impurities are negligible. We also note that the synthesis C_M values have no clear effect on the lattice parameters. Manthiram et al.,[33] Chen et al.,[18] and Younesi et al.[44] have shown that the materials synthesized by low temperature processes as sol–gel or hydrothermal reactions show better electrochemical performance after high temperature annealing, indicating that there are possibly

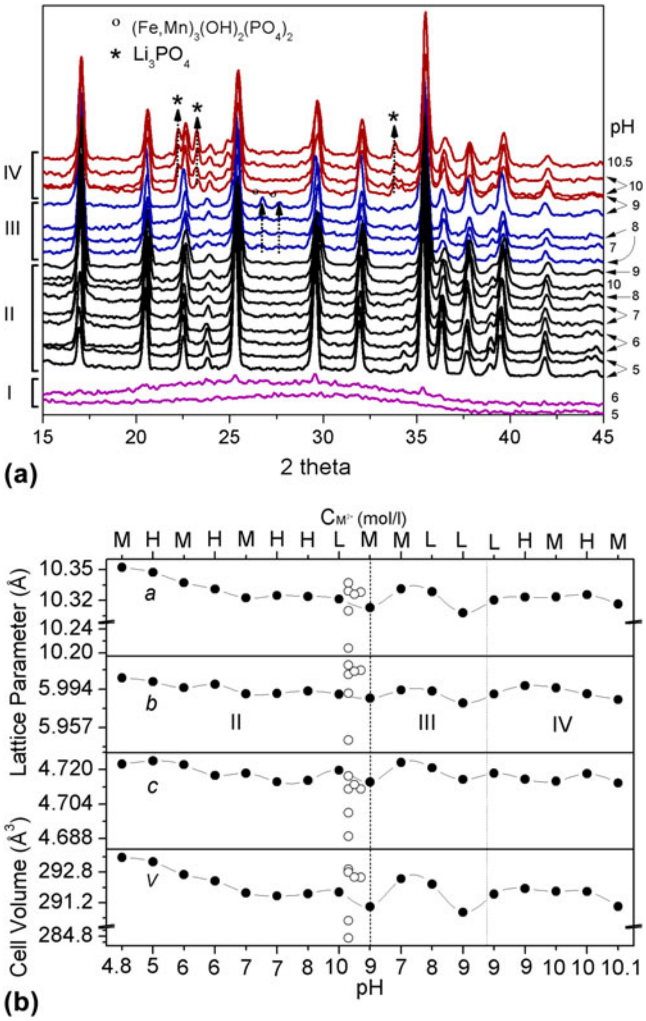

FIG. 2. (a) XRD patterns of the as-prepared LFMC samples. Left: regimes I–IV (see the text and Fig. 3), right: pH-values at which the synthesis was done, (b) comparison of the lattice parameters and unit cell volumes of our samples made at different pH and C_M values (solid circles) with literature data (open circles, see the text). Synthesis regions with pure LFMC (II), LFMC with $(Fe,Mn)_3(OH)_2(PO_4)_2$ impurities (III), and LFMC with Li_3PO_4 impurities (IV) are separated by the two dashed lines.

defects in these materials prior to annealing. Therefore, we assume that the lattice parameters of our samples might be reverted to the normal values and the electrochemistry performance could be improved after additional thermal treatment.

To assess the growth mechanism and to draw conclusions regarding the relation of synthesis conditions to shape and morphology of the products, the morphology of the olivine-structured LFMC crystals is quantitatively analyzed from first principle calculations, using the Hartman–Perdok approach.[45] In general, the external morphology of a crystal is determined by its internal crystal structure, by the growth conditions, and by the potential presence of impurities. Based on the work of Bravais, Friedel, Donnay, and Harker (BFDH), predictions of the morphology of grown crystals can be made by considering the respective geometry of the crystal lattice.[46] For such simulation, it is supposed that the larger the interplanar distance d_{hkl} of a crystal face $\{hkl\}$ is, the more relevant $\{hkl\}$ is for the crystal morphology. From this supposition, a series of possible growth faces $\{hkl\}$ can be determined from the crystal lattice symmetry. For LFMC, the morphologically most relevant growth forms are {200}, {101}, {210}, {011}, {111}, and {020}. Hence, the BFDH law predicts that the most important crystal growth forms of LFMC are the pinacoids {200} and {020}, followed by the orthorhombic prisms {101}, {210}, and {011}, and the tetragonal dipyramid {111}. All these forms are shown in Fig. 4(a), which displays a Wulff plot generated from the BFDH list of faces and center-to-face distances. This result can be compared to the size and shape of the actually grown material as seen in the SEM images for selected phase-pure LFMC samples in Fig. 5. The SEM images show three general kinds of single particles with regular external shapes as seen in Figs. 5-M2, 5-M3b, and 5-M3c, respectively. In the images, layered growth traces on the surface possibly initiated from step sources are clearly observed, indicating a single crystalline nature of the primary particles. In the following, we compare the predicted morphologies from the Wulff plot simulation of the BFDH morphology, as displayed in Fig. 4, with the actual SEM images. The single crystal with rhombic shape (Fig. 5-M3b) is formed by the pinacoid {200} followed by the orthorhombic prism {011}, while the square shape [e.g., Figs. 5-M3c and 5-M2] is formed by the pinacoid{020} followed by the orthorhombic prism {101}. In addition to the above-mentioned simulations, the Miller indices of the existing faces can be determined by applying the law of constancy of interfacial angles as well. The images in Fig. 5 show that the {200}, {101}, {011}, and {020} faces are

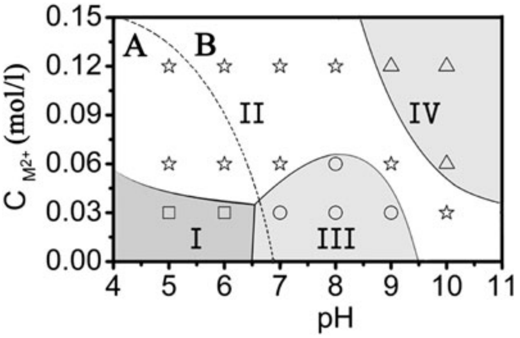

FIG. 3. Crystalline and agglomeration phase diagram with respect to the pH and C_M values. I: noncrystalline phase marked with squares, II: pure LFMC marked with stars, III: LFMC with $(Fe,Mn)_3(OH)_2(PO_4)_2$ impurities marked with circles, and IV: LFMC with Li_3PO_4 impurities marked with triangles. The dominating continuous single crystal growth route (labeled A) and the agglomeration route (labeled B) are separated by the two dashed lines.

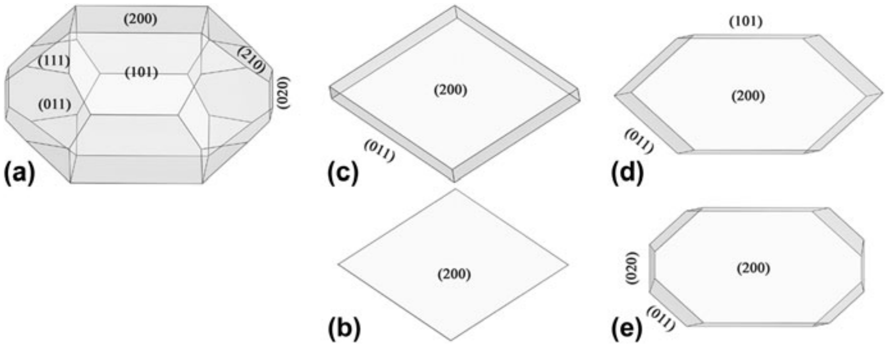

FIG. 4. Predicted morphologies (a) from Wulff plot simulations applying the BFDH law, and (b–e) from the attachment energy model of Hartman and Perdok theory (HPT).

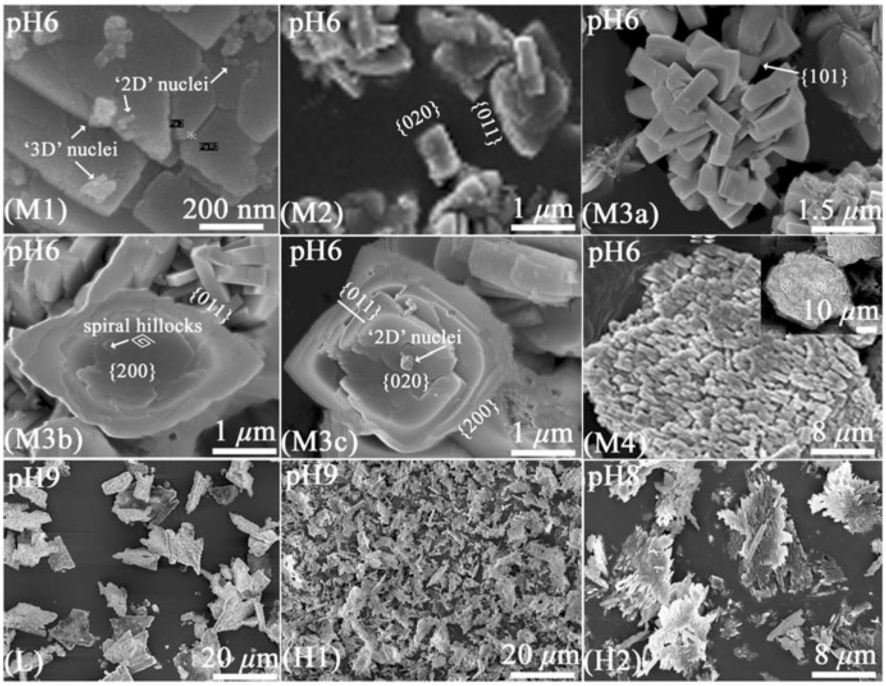

FIG. 5. SEM images of LFMC obtained under different pH values (see the text) and M-ion concentrations (C_M). **L**: $C_M = 0.03$ mol/L; **M**: $C_M = 0.06$ mol/L; **H**: $C_M = 0.12$ mol/L.

developed whereas the {210} and {111} faces are not observed in our experiments, which is in contrast to the predictions of the basic BFDH simulations.

Hence, to predict the shape of a crystal more accurately, the energy of the system must be taken into account. Most notably, the attachment energy model of Hartman and Perdok[47] makes use of the actual magnitude of molecular interactions to estimate the relative growth rates of crystal faces. In this model, the growth rate of a crystal face is assumed to be proportional to its attachment energy, i.e., faces with the lowest attachment energies are the slowest growing ones and, therefore, have the highest morphological relevance. The attachment energy E_{att} is defined as the energy released on attachment of a growth slice to a growing crystal surface. E_{att} is computed as: $E_{att} = E_{latt}–E_{slice}$, where E_{latt} is the lattice energy of the crystal, E_{slice} is the energy of a growth slice with thickness d_{hkl}, and the growth rate is proportional to E_{att}. The attachment energy method attempts to obtain crystal habits under nonequilibrium growth conditions by simulation. In our work, the attachment energy is calculated based on the first principle method for a series of slices $\{hkl\}$ that we have determined by performing a Donnay–Harker prediction.

The Hartman–Perdok approach starts with the search of periodic bond chains (PBCs), which are uninterrupted periodic chains of strong bonds between the crystalline units, such as atoms, molecules, or clusters, formed during crystallization. Crystal faces can be classified either as F faces, which contain at least two nonparallel PBCs in a slice of thickness d_{hkl}, or as S faces containing only one PBC, or as K faces containing no PBC at all. The F faces are the slowest to grow according to the layer mechanism and therefore are the dominant faces present on actual growth forms. According to the crystal structure of LFMC [Fig. 1(a)], five main PBCs can be traced, which are shown in Fig. 6. They can be represented by the following crystal directions:

$$\begin{aligned}<001>: &\mathrm{Li}(x,y,z) - \mathrm{PO_4}(x,y,z) - \mathrm{M}(x,y,z-1)\\ &- \mathrm{PO_4}(x+1/2,-y+1/2,-z+1/2)\\ &- \mathrm{Li}(x+1,y,z) \quad ,\end{aligned}$$

$$\begin{aligned}<010>: &\mathrm{Li}(x,y,z) - \mathrm{M}(x-1/2,-y+1/2,-z+3/2)\\ &- \mathrm{Li}(-x,y+1/2,-z)\\ &- \mathrm{PO_4}(-x,y+1/2,-z+1)\\ &- \mathrm{Li}(x,y+1,z) \quad ,\end{aligned}$$

$$\begin{aligned}<011>: &\mathrm{Li}(x,y,z) - \mathrm{PO_4}(x,y,z) - \mathrm{PO_4}(-x,y+1/2,-z+1)\\ &- \mathrm{Li}(x,y+1,z+1) \quad ,\end{aligned}$$

$$\begin{aligned}<0-11>: &\mathrm{Li}(x,y,z) - \mathrm{PO_4}(-x,y-1/2,-z+1)\\ &- \mathrm{PO_4}(x,y-1,z) - \mathrm{Li}(x,y-1,z+1) \quad ,\end{aligned}$$

$$\begin{aligned}<100>: &\mathrm{PO_4}(x,y,z) - \mathrm{Li}(-x+1/2,-y,z+1/2)\\ &- \mathrm{PO_4}(x+1/2,-y+1/2,-z+1/2)\\ &- \mathrm{M}(x+1/2,-y+1/2,-z+3/2)\\ &- \mathrm{PO_4}(x+1,y,z) \quad .\end{aligned}$$

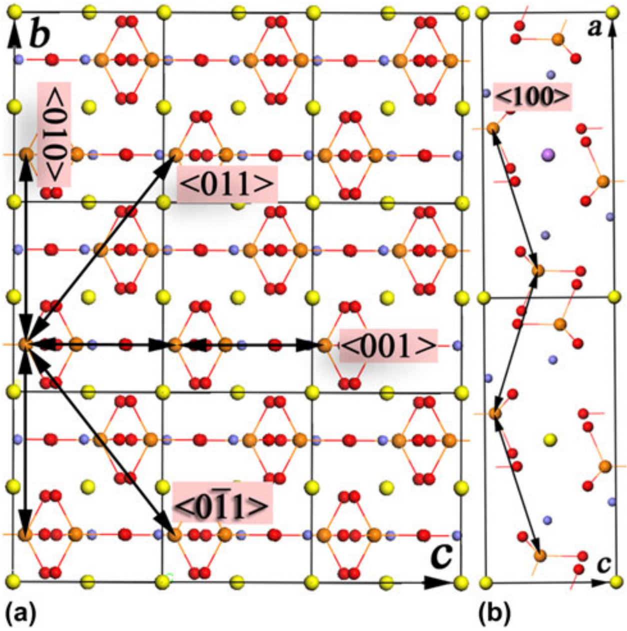

FIG. 6. The main PBCs in LFMC (a) <010>, <001>, <011>, and $\langle 0\bar{1}1\rangle$ parallel to the {200} slices and (b) <100> parallel to the {010} slices.

Table I lists the {*hkl*} faces of the grown crystal, their interplanar distances d_{hkl}, the calculated attachment energies (E_{att}), and the PBCs parallel to the {*hkl*} faces. From Table I, we can see that four F faces can be defined, which have at least two noncollinear PBCs within their corresponding slice boundaries with a thickness of d_{hkl}. Among them, the {200} faces are parallel to four strong PBCs, <001>, <010>, <011>, and $\langle 0\bar{1}1\rangle$; the {101} faces are parallel to <010> and $\langle 10\bar{1}\rangle$; the {011} faces are parallel to $\langle 0\bar{1}1\rangle$ and <100>; and the {020} faces are parallel to <001> and <100>, respectively. Furthermore, the {210} and {111} faces are parallel to only one strong PBC, which defines them as S faces. Generally, the F faces of crystals are well developed, since there are no strong PBCs running across these faces, and therefore they have a slow growth rate. However, S faces only appear in certain as-grown crystals because only one strong PBC is parallel to them and their fast growth rate can be easily disturbed by dynamic factors of the crystal growth.

From the calculated attachment energies, we suggest that the order of morphological relevance of the different faces should be {200} > {011} > {101} > {020}. Indeed, in our experiments, the {200} and {011} faces are usually well developed [see Figs. 5-M3b and 5-M3c], while the {020} faces appear only rather occasionally [see Figs. 5-M2 and 5-M3c].

Our analysis suggests that two evolutionary routes are involved in the forming process of the LFMC powder samples. In the early stage of the growth process, “2D-nuclei” as well as “3D-nuclei” are formed [Fig. 5-M1], initially driven by a localized supersaturation ($\sigma \sim C_{\mathrm{M}}$).[48] In particular, the “2D-nuclei” can be related to the layer-like growth of the {200} and {020} faces, apparent in Figs. 5-M3b and 5-M3c. Both kinds of nuclei grow larger by the attachment of atoms to edges and kinks of growing surfaces.[49] In the following, we will refer to this process as route A, i.e., the continuous growth of primary particles. With increasing volume of the particles, additional {011} faces appear [Figs. 4(c) and 5-M2]. The final morphologies vary a lot depending on whether the {101} faces appear or not. The crystals without {101} faces tend to form rhombic and square shapes [Figs. 5-M3b and 5-M3c], as predicted in Fig. 4(c) for the former case. In addition to the individual growth, the primary particles agglomerate due to Van der Waals and Coulomb forces which is referred to as route B, i.e., agglomeration. The outcome of this process is seen in Fig. 5 from M2 to M4. The two evolutionary routes A and B coexist and compete with each other after a stable “3D-nucleus” is formed. The morphological variety of the products may hence be associated with the competition between the two routes, depending on pH and C_{M}. Indeed, the dominating regimes of routes A and B can be separated in the phase diagram, which is illustrated by the

TABLE I. {*hkl*} faces of the grown LFMC crystals, their attachment energy E_{att}, interplanar distances d_{hkl}, PBCs parallel to them, and the experimentally observed faces.

			Main PBCs bonds and their periods (Å)					
{*hkl*}	d_{hkl} (Å)	E_{att} (kcal/mol)	4.700	5.989	7.613	7.613	5.392	Experimental observed
{200}	5.1535	−630.15	<001>	<010>	<011>	$\langle 0\bar{1}1\rangle$	...	Yes
{101}	4.2764	−118.39	...	<010>	$\langle 10\bar{1}\rangle$	...	...	Yes
{210}	3.9063	−19.96	<001>	...	...	...	...	No
{011}	3.6974	−293.54	...	...	...	$\langle 0\bar{1}1\rangle$	<100>	Yes
{111}	3.4802	−12.15	...	...	...	$\langle 01\bar{1}\rangle$	...	No
{020}	2.9945	−103.51	<001>	...	...	...	<100>	Yes

dashed line in Fig. 3. High C_M is favorable for agglomeration, whereas low C_M favors the continuous single particle growth. The dominance of route A at $pH < 7$ may be explained by the acidity of the solution which induces positively charged surfaces and hence inhibits agglomeration of the primary particles. At $pH = 6$ and $C_M = 0.06$ mol/L, single particles can be observed in different growth states from "2D-nuclei" with sizes of ~40 nm [Fig. 5-M1], crystallites up to 700 nm [Fig. 5-M2], to several μm long crystals [Figs. 5-M3b and 5-M3c]. The size of the rhombic-shaped crystals [Fig. 5-M3b] and the square-formed single crystals [Fig. 5-M3c] is about 4.5 × 3.3 μm and 2.7 × 2.7 μm, respectively. One factor for the dominance of route B in the corresponding synthesis regime could be the occurrence of the {101} face. As evident from Fig. 1(b), the {101} surface terminates with either positively charged Li^+ or negatively charged O^{2-}. Under these circumstances, strong chemical bonds can be formed between the Li^+-charged {101} surfaces of one primary particle and the O^{2-}-charged {101} surfaces of another one in the reaction solution. If, however, {101} faces do not appear, the aforementioned single particle growth forms mainly prevail because there is no facilitation of agglomeration by oppositely charged surfaces. The size of aggregates at $pH = 6$ ranges from ~5.5 μm [Fig. 5-M3a] to 17 μm [Fig. 5-M4] up to ~43 μm [inset in Fig. 5-M4] at $C_M = 0.12$ mol/L. The largest primary particles at the highest precursor concentration are only ~0.3 μm big because route A is suppressed by the dominating route B. At $pH = 9$, the largest single crystallites are ~0.3 × 0.1 μm and the observed aggregates are ~10 μm big. Figure 5-M3a shows the same morphology with the traditional hydrothermal formed LFMC heated at 200 °C for two days using ascorbic acid as the reductant.[18]

In summary, route A ("continuous growth") dominates the process at low C_M and low pH value, while route B ("agglomeration") prevails at high C_M and/or high pH value. Quantitatively, dispersed crystals appear at $pH < \sim 7$ while a strong tendency to agglomeration is found at $pH > \sim 7$. The results hence imply the isoelectric point of LFMC being around pH 7.

B. Magnetic properties

Figure 7 shows the temperature dependence of the static magnetic susceptibility and its inverse of a typical LFMC sample (i.e., from regime II in Fig. 3) at temperatures between 2 and 350 K, measured in an external magnetic field of $B = 0.5$ T. The data show paramagnetic Curie–Weiss-like behavior at high temperatures and a long range antiferromagnetically ordered ground state. The susceptibility peak maximum appears at 39.0(5) K. The magnetic specific heat $c_{magn} \sim \partial(\chi T)/\partial T$ exhibits a pronounced lambda-like maximum from which we deduce $T_N = 33.0(5)$ K. At high temperatures, the data are well described by the modified Curie–Weiss law $\chi(T) = \chi_0 + C/(T - \theta)$, with Curie constant C, Weiss temperature θ, and a temperature-independent contribution $\chi_0 = -3 \times 10^{-4}$ emu/(G^2 mol). T_N as well as the extracted Curie temperature $\theta = -75(5)$ K are in between the respective values of the pure compounds $LiMPO_4$ with M = Fe ($T_N \approx 52$ K, $\theta \approx -120$ K), M = Co (≈21 K, ≈−52 K), and M = Mn (≈34 K, ≈−65 K).[50–56] The effective magnetic moment of the M^{2+}-ions deduced from the Curie–Weiss analysis amounts to $p_{eff} = 5.51(2)$ μ_B. This value agrees well with the value of 5.47 μ_B which is theoretically predicted if the spin and a reduced (pseudo-) orbital momentum $l = 1$ are considered. The latter reflects partial quenching of the orbital momentum of electrons in t_{2g}–orbital states by the crystal field.

C. Electrochemical properties

The electrochemical properties are studied by CV in the potential range between 2.60 and 5.25 V at a scan rate of 0.1 mV s^{-1}. Figure 8 shows the CV curve of one exemplary sample, synthesized at pH 9 and $C_M = 0.12$ mol/L, consisting of highly agglomerated rods with sub-μm dimensions. The data show two distinct areas of electrochemical activity with redox pairs at 3.6 V/3.1 V and 4.9 V/4.6 V, which are most likely associated with the oxidation/reduction of Fe^{2+}/Fe^{3+} and Co^{2+}/Co^{3+}, respectively. At potentials exceeding 4.5 V, there is also a strong irreversible

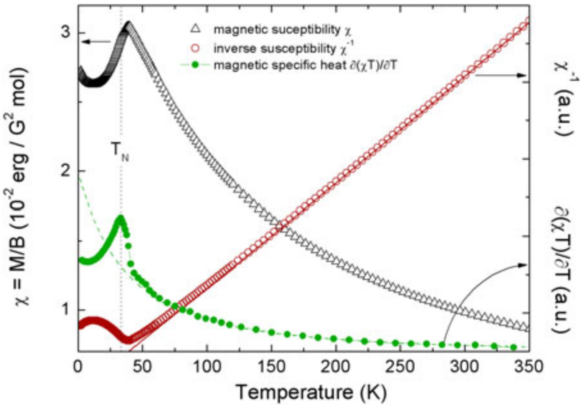

FIG. 7. Temperature dependence of the static magnetic susceptibility *M*/*B* (left ordinate), the inverse susceptibility, and the magnetic specific heat (both right ordinate) of LFMC from 2 to 350 K measured at $B = 0.5$ T. Lines reflect a Curie–Weiss approximation, T_N has been deduced from the magnetic specific heat $\partial(\chi T)/\partial T$ (see the text).

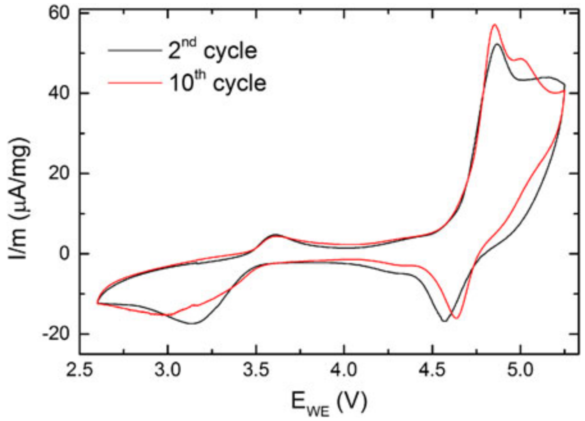

FIG. 8. Exemplary CV curve of one sample synthesized at pH 9 and C_M 0.12 mol/L, showing Fe^{2+}/Fe^{3+} and Co^{2+}/Co^{3+} redox peaks at 3.6 V/3.1 V and 4.9 V/4.6 V respectively.

oxidative contribution caused by electrolyte decomposition,[15] which partially overlays the Co^{2+}/Co^{3+} oxidation. Nevertheless, the Co^{2+}/Co^{3+} activity is significant, as evident from the pronounced reduction peak at 4.6 V. The absence of visible Mn^{2+}/Mn^{3+} redox peaks in the CV, expected in the potential range around 4.1 V, is probably due to the sluggish kinetics of the Mn^{2+}/Mn^{3+} couple, induced by the Jahn–Teller effect of Mn^{3+}.[11,56]

The work of Zhang et al.[20] shows electrochemical activity of all redox couples in $LiFe_{1/3}Mn_{1/3}Co_{1/3}PO_4$ with increasing working potentials for Fe^{2+}/Fe^{3+} and decreasing ones for Co^{2+}/Co^{3+}. We cannot draw accordant conclusions because our pristine materials still suffer from the low intrinsic electronic conductivity and ionic diffusivity of the olivine-type phosphates. In particular, this is reflected in the huge overpotential gap between the Fe^{2+}/Fe^{3+} oxidation and reduction peak and the broadening of the latter one. We emphasize in this context that the materials used for our electrochemical characterization were not subject to carbon coating or any postsynthesis treatment as the present work aims at elucidating growth mechanisms and morphology-related effects. Furthermore, all synthesized samples either show particle dimensions >1 μm or are part of agglomerates of several μm sizes (see Sec. III. A), which lead to quite similar results in CVs.

IV. CONCLUSIONS

We report the synthesis of $LiFe_{1/3}Mn_{1/3}Co_{1/3}PO_4$ by using the microwave-assisted hydrothermal technique at different pH and different transition-metal-ion concentrations in the reactant. The morphology of the products has been analyzed by first principle calculations using the Hartman–Perdok approach, which are discussed against actual size and shape of the produced materials. The growth mechanism under different pH and C_M values is discussed. In addition, the magnetic properties of the products are studied and the electrochemical properties are initially evaluated by the CV measurements.

ACKNOWLEDGMENTS

The authors thank I. Glass for experimental assistance. Support by the Bundesministerium für Bildung und Forschung (project 03SF0397) and by Deutsche Forschungsgemeinschaft (KL1824/2, KL1824/5) is gratefully acknowledged. KW acknowledges support by the European Commission through FP7 Marie Curie Grant PIIF-GA-2012-331476 LiCrystG.

REFERENCES

1. J.M. Tarascon and M. Armand: Issues and challenges facing rechargeable lithium batteries. *Nature* **414**, 359 (2001).
2. M.S. Whittingham: Lithium batteries and cathode materials. *Chem. Rev.* **104**, 4271 (2004).
3. J.B. Goodenough and Y. Kim: Challenges for rechargeable Li batteries. *Chem. Mater.* **22**, 587 (2010).
4. J.B. Goodenough: Cathode materials: A personal perspective. *J. Power Sources* **174**, 996 (2007).
5. A.K. Padhi, K.S. Nanjundaswamy, and J.B. Goodenough: Phospho-olivines as positive-electrode materials for rechargeable lithium batteries. *J. Electrochem. Soc.* **144**, 1188 (1997).
6. A. Yamada, M. Hosoya, S.C. Chung, Y. Kudo, K. Kinokuma, K.Y. Liu, and Y. Nishi: Olivine-type cathodes: Achievements and problems. *J. Power Sources* **119**, 232 (2003).
7. K. Amine, H. Yasuda, and M. Yamachi: Olivine $LiCoPO_4$ as 4.8 V electrode material for lithium batteries. *Electrochem. Solid-State Lett.* **3**, 178 (2000).
8. J. Wolfenstine and J. Allen: Ni^{3+}/Ni^{2+} redox potential in $LiNiPO_4$. *J. Power Sources* **142**, 389 (2005).
9. H. Huang, S.C. Yin, and L.F. Nazar: Approaching theoretical capacity of $LiFePO_4$ at room temperature at high rates. *Electrochem. Solid-State Lett.* **4**, A170 (2001).
10. D. Zane, M. Carewska, S. Scaccia, F. Cardellini, and P.P. Prosini: Factor affecting rate performance of undoped $LiFePO_4$. *Electrochim. Acta.* **49**, 4259 (2004).

11. M. Yonemura, A. Yamada, Y. Takei, N. Sonoyama, and R. Kanno: Comparative kinetic study of olivine Li_xMPO_4 (M = Fe, Mn). *J. Electrochem. Soc.* **151**, A1352 (2004).
12. C. Rudisch, H.J. Grafe, J. Geck, S. Partzsch, M.V. Zimmermann, N. Wizent, R. Klingeler, and B. Büchner: Coupling of Li motion and structural distortions in olivine $LiMnPO_4$ from ^{7}Li and ^{31}P NMR. *Phys. Rev. B* **88**, 054303 (2013).
13. H.H. Li, J. Jin, J.P. Wei, Z. Zhou, and J. Yan: Fast synthesis of core-shell $LiCoPO_4$/C nanocomposite via microwave heating and its electrochemical Li intercalation performances. *Electrochem. Commun.* **11**, 95 (2009).
14. J. Wolfenstine and J. Allen: $LiNiPO_4$–$LiCoPO_4$ solid solutions as cathodes. *J. Power Sources* **136**, 150 (2004).
15. K. Xu: Nonaqueous liquid electrolytes for lithium-based rechargeable batteries. *Chem. Rev.* **104**, 4303 (2004).
16. A. Yamada, Y. Takei, H. Koizumi, N. Sonoyama, and R. Kanno: Electrochemical, magnetic, and structural investigation of the $Li_x(Mn_yFe_{1-y})PO_4$ olivine phases. *Chem. Mater.* **18**, 804 (2006).
17. A. Yamada, Y. Kudo, and K.Y. Liu: Reaction mechanism of the olivine-type $Lix(Mn_{0.6}Fe_{0.4})PO_4$ ($0 \leq x \leq 1$). *J. Electrochem. Soc.* **148**, A747 (2001).
18. J. Chen, M.J. Vacchio, S. Wang, N. Chernova, P.Y. Zavalij, and M.S. Whittingham: The hydrothermal synthesis and characterization of olivines and related compounds for electrochemical applications. *Solid State Ionics* **178**, 1676 (2008).
19. H. Gwon, D.H. Seo, S.W. Kim, J. Kim, and K. Kang: Combined first-principle calculations and experimental study on multi-component olivine cathode for lithium rechargeable batteries. *Adv. Funct. Mater.* **19**, 3285 (2009).
20. Y. Zhang, C.S. Sun, and Z. Zhou: Sol–gel preparation and electrochemical performances of $LiFe_{1/3}Mn_{1/3}Co_{1/3}PO_4$/C composites with core–shell nanostructure. *Electrochem. Commun.* **11**, 1183 (2009).
21. Y.C. Chen, J.M. Chen, C.H. Hsu, J.J. Lee, T.C. Lin, J.W. Yeh, and H.C. Shih: Electrochemical and structural studies of $LiCo_{1/3}Mn_{1/3}Fe_{1/3}PO_4$ as a cathode material for lithium ion batteries. *J. Power Sources* **195**, 6867 (2010).
22. M. Yoshimura and K. Byrappa: Hydrothermal processing of materials: Past, present and future. *J. Mater. Sci.* **43**, 2085 (2008).
23. S. Yang, P.Y. Zavalij, and M. Whittingham: Hydrothermal synthesis of lithium iron phosphate cathodes. *Electrochem. Commun.* **3**, 505 (2001).
24. J. Chen, S. Wang, and M. Whittingham: Hydrothermal synthesis of cathode materials. *J. Power Sources* **174**, 442 (2007).
25. C. Delacourt, P. Poizot, M. Morcrette, J.M. Tarascon, and C. Masquelier: One-step low-temperature route for the preparation of electrochemically active $LiMnPO_4$ powders. *Chem. Mater.* **16**, 93 (2004).
26. K. Dokko, S. Koizumi, H. Koizumi, and K. Kanamura: Particle morphology, crystal orientation, and electrochemical reactivity of $LiFePO_4$ synthesized by the hydrothermal method at 443 K. *J. Mater. Chem.* **17**, 4803 (2007).
27. N. Recham, M. Armand, L. Laffont, and J.M. Tarascon: Eco-efficient synthesis of $LiFePO_4$ with different morphologies for Li-ion batteries. *Electrochem. Solid-State Lett.* **12**, A39 (2009).
28. C. Neef, C. Jähne, H-P. Meyer, and R. Klingeler: Morphology and agglomeration control of $LiMnPO_4$ micro- and nanocrystals. *Langmuir* **29**, 8054 (2013).
29. C. Jähne, R. Klingeler: Microwave-assisted and conventional hydrothermal synthesis. *Solid State Sci.* **14**, 941 (2012).
30. Y.Q. Wang, D.Y. Zhang, C.K. Chang, L. Deng, and K.J. Huang: Controllable growth of $LiFePO_4$ microplates of (010) and (001) lattice planes for Li ion batteries: A case of the growth manner on the Li ion diffusion coefficient and electrochemical performance. *Mater. Chem. Phys.* **148**, 933 (2014).
31. X.J. Huang, S.J. Yan, H.Y. Zhao, L. Zhang, R. Guo, C.K. Chang, X.Y. Kong, and H.B. Han: Electrochemical performance of $LiFePO_4$ nanorods obtained from hydrothermal process. *Mater. Charact.* **61**, 720 (2010).
32. I. Bilecka and M. Niederberger: Microwave chemistry for inorganic nanomaterials synthesis. *Nanoscale* **2**, 1358 (2010).
33. A. Manthiram, A.V. Murugan, A. Sarkar, and T. Muraliganth: Nanostructured electrode materials for electrochemical energy storage and conversion. *Energy Environ. Sci.* **1**, 621 (2008).
34. A.V. Murugan, T. Muraliganth, P.J. Ferreira, and A. Manthiram: Dimensionally modulated, single-crystalline $LiMPO_4$ (M = Mn, Fe, Co and Ni) with nano-thumblike shapes for high-power energy storage. *Inorg. Chem.* **48**, 946 (2009).
35. C. Jähne, C. Neef, C. Koo, H-P. Meyer, and R. Klingeler: A new $LiCoPO_4$ polymorph via low temperature synthesis. *J. Mater. Chem. A* **1**, 2856 (2013).
36. M.C. Payne, M.P. Teter, D.C. Allan, T.A. Arias, and J.D. Joannopoulos: Iterative minimization techniques for ab initio total-energy calculations: Molecular dynamics and conjugate gradients. *Rev. Mod. Phys.* **64**, 1045 (1992).
37. D. Vanderbilt: Soft self-consistent pseudopotentials in a generalized eigenvalue formalism. *Phys. Rev. B* **41**, 7892 (1990).
38. K.P. Wang, C.S. Fang, J.X. Zhang, C.S. Liu, R.I. Boughton, S.L. Wang, and X. Zhao: First-principles study of interstitial oxygen in potassium dihydrogen phosphate crystals. *Phys. Rev. B* **72**, 184105 (2005).
39. J.P. Perdew, K. Burke, and M. Ernzerhof: Generalized gradient approximation made simple. *Phys. Rev. Lett.* **77**, 3865 (1996).
40. A. Majchrowski, M.T. Borowiec, and E.J. Michalski: Top seeded solution growth of $KHo(WO_4)_2$ single crystals. *J. Cryst. Growth* **264**, 201 (2004).
41. A.C. Larson and R.B. Dreele: *General Structure Analysis System (GSAS)*, Los Alamos National Laboratory Report LAUR, 1994; p. 86.
42. Y. Park, J. Kim, H. Gwon, D.H. Seo, S.W. Kim, and K. Kang: Synthesis of multicomponent olivine by a novel mixed transition metal oxalate coprecipitation method and electrochemical characterization. *Chem. Mater.* **22**, 2573 (2010).
43. X.J. Wang, X.Q. Yu, H. Li, X.Q. Yang, J. Mcbreen, and X.J. Huang: Li-storage in $LiFe_{1/4}Mn_{1/4}Co_{1/4}Ni_{1/4}PO_4$ solid solution. *Electrochem. Commun.* **10**, 1347 (2008).
44. R. Younesi, S. Malmgren, K. Edström, and S. Tan: Influence of annealing temperature on the electrochemical and surface properties of the 5-V spinel cathode material $LiCr_{0.2}Ni_{0.4}Mn_{1.4}O_4$ synthesized by a sol–gel technique. *J. Solid State Electrochem.* **18**, 2157 (2014).
45. P. Hartman and W.G. Perdok: On the relations between structure and morphology of crystals. I. *Acta Cryst.* **8**, 49 (1955).
46. R. Docherty, G. Clydesdale, K.J. Roberts, and P. Bennema: Application of Bravais-Friedel-Donnay-Harker, attachment energy and Ising models to predicting and understanding the morphology of molecular crystals. *J. Phys. D: Appl. Phys.* **24**, 89 (1991).
47. R. Dekkers and C.F. Woensdregt: Crystal structural control on surface topology and crystal morphology of normal spinel ($MgAl_2O_4$). *J. Cryst. Growth* **236**, 441 (2002).
48. K.P. Wang, D.L. Sun, J.X. Zhang, W.T. Yu, H. Liu, X.B. Hu, S.Y. Guo, and Y.L. Geng: Spiral growth mechanisms of CMTD crystals. *J. Cryst. Growth* **261**, 63 (2004).
49. K.P. Wang, J.X. Zhang, J.Y. Wang, W.T. Yu, H.J. Zhang, Z.P. Wang, and M.F. Ba: Investigation of growth mechanisms of TSS-grown $KLu(WO_4)_2$ crystals by atomic force microscopy. *Opt. Mater.* **29**, 421 (2006).
50. D.P. Chen, X. Wang, Y.S. Hu, C.T. Lin, S.X. Dou, and R. Nigam: Magnetic anisotropy in doped and undoped $LiFePO_4$ single crystals. *J. Appl. Phys.* **101**, 09N512 (2007).

51. R.P. Santoro and R.E. Newnham: Antiferromagnetism in $LiFePO_4$. *Acta Crystallogr.* **22**, 344 (1967).
52. A. Szewczyk, M.U. Gutowska, J. Wieckowski, A. Wisniewski, R. Puzniak, R. Diduszko, Yu. Kharchenko, M.F. Kharchenko, and H. Schmid: Phase transitions in single-crystalline magnetoelectric $LiCoPO_4$. *Phys. Rev. B* **84**, 104419 (2011).
53. S.H. Baek, R. Klingeler, C. Neef, C. Koo, B. Büchner, and H.J. Grafe: Unusual spin fluctuations and magnetic frustration in olivine and non-olivine $LiCoPO_4$ detected by ^{31}P and ^{7}Li nuclear magnetic resonance. *Phys. Rev. B* **89**, 134424 (2014).
54. N. Wizent, G. Behr, F. Lipps, I. Hellmann, R. Klingeler, V. Kataev, W. Löser, N. Sato, and N. Büchner: Single-crystal growth of $LiMnPO_4$ by the floating-zone method. *J Cryst Growth.* **311**, 1273 (2009).
55. R.P. Santoro, D.J. Segal, and R.E. Newnham: Magnetic properties of $LiCoPO_4$ and $LiNiPO_4$. *J. Phys. Chem. Solids* **27**, 1192 (1966).
56. Z. Nie, C. Ouyang, J. Chen, Z. Zhong, Y. Du, D. Liu, S. Shi, and M. Lei: First principles study of Jahn–Teller effects in Li_xMnPO_4. *Solid State Commun.* **150**, 40 (2010).